Origin of Nonlinear Damping Due to Mode Coupling in Auto-Oscillatory Modes Strongly Driven by Spin-Orbit Torque

Inhee Lee [●],[*] Chi Zhang, Simranjeet Singh,[‡] Brendan McCullian [●], and P. Chris Hammel [●][†]

Department of Physics, The Ohio State University, Columbus, Ohio 43210, USA

We investigate the physical origin of nonlinear damping due to mode coupling between several auto-oscillatory modes driven by spin-orbit torque in constricted Pt/Py(permalloy) heterostructures by examining the dependence of the auto-oscillation on the temperature and the applied field orientation. We observe a transition in the nonlinear damping of the auto-oscillation modes extracted from the total oscillation power as a function of the drive current, which coincides with the onset of power redistribution among several modes and the crossover from linewidth narrowing to linewidth broadening in all individual modes. This indicates the activation of another relaxation process by nonlinear magnon-magnon scattering within the modes. We also find that both nonlinear damping and the threshold current in the mode-interaction damping regime at high drive current after transition are temperature independent, suggesting that the mode coupling occurs dominantly through a nonthermal magnon-scattering process via a dipole or exchange interaction rather than thermally excited magnon-mediated scattering. This finding presents a promising pathway toward overcoming the current limitations of efficiently controlling the interaction between two highly nonlinear magnetic oscillators to prevent mode crosstalk or intermode energy transfer and deepens the understanding of complex nonlinear spin dynamics in multimode spin-wave systems.

I. INTRODUCTION

Spin-orbit torque driven magnetic nano-oscillators have recently emerged as potential charge-current tunable microwave sources for spintronics devices [1–13], as well as fundamental elements for neuromorphic computing [14]. These oscillators use the spin Hall effect to convert the charge current into a pure spin current that is injected into the ferromagnet, exerting an antidamping torque on the magnetization. Above the threshold current, coherent magnetic auto-oscillations (AOs) are generated at microwave frequencies.

In principle, these planar spin Hall nano-oscillators (SHNOs) need not be limited in size and are expected to provide larger AO power because the Oersted field is relatively small and uniform in the device, unlike nanopillar spin-torque nano-oscillators (STNOs). However, additional damping channels arise in extended thin-film structures through nonlinear magnon scattering that prevents auto-oscillation [4]. These damping channels can be suppressed by restricting the area of the AO by fabricating a nanoconstriction [3,10] as well as other methods of

spatial mode confinement, such as dimensional reduction [4,15] and local dipolar field [16–19].

Nevertheless, in constriction-based SHNOs, mode splittings are often observed [3,10], leading to substantial linewidth broadening that degrades performance in terms of AO coherence and power. So far, little is known about the origins of nonlinear damping as a consequence of multimode excitation in this system and the mechanism underlying mode coupling is still unknown. In nanopillar STNOs, similar multimode behaviors such as mode hopping [20–26], mode coexistence [27–29], and the three-magnon process [30,31], have been reported along with theoretical studies [20–26,29,32,33] of mode coupling, including its description [21–26,33], its effect on mode decoherence [22,24,25], and its temperature dependence [22,24,25,33], however, much remains to be understood.

II. EXPERIMENT AND RESULTS

For this study, we fabricate Pt(5 nm)/Py(5 nm) bilayer devices in the form of a bow tie with an active center area of 600 nm × 1 μm, as shown in Fig. 1(a). This sample structure allows the generation of multiple AO modes by applying a high current density J_c that is converted into a spin current J_s that, in turn, exerts a spin torque on the magnetization of the Py [see Fig. 1(b)]. By changing the orientation of the magnetic field $\mathbf{H_0}$ applied at angle θ with

---

[*]lee.2338@osu.edu

[†]hammel@physics.osu.edu

[‡]Present address: Department of Physics, Carnegie Mellon University, Pittsburgh, Pennsylvania 15213, USA.
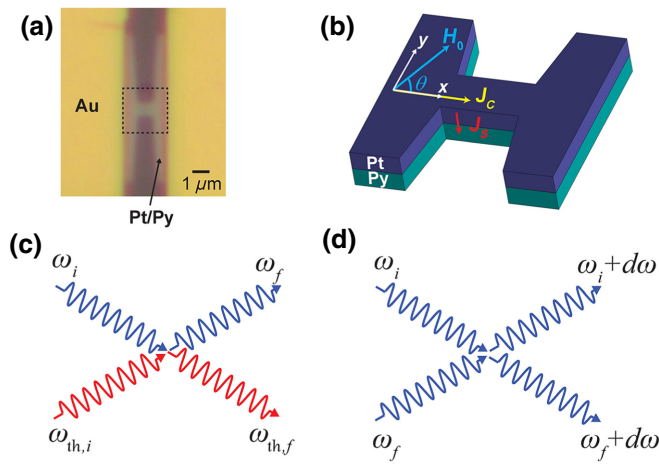
FIG. 1. (a) An optical image of the auto-oscillation device. (b) A schematic diagram of the two-dimensionally (2D) constricted Pt(5 nm)/Py(5 nm) bilayer structure of the bow-tie shape in the dashed box of (a). Due to the strong spin-orbit coupling in Pt, the charge-current density $\mathbf{J_c}$ flowing in the x direction along the axis of the microstrip line is converted to pure spin-current density $\mathbf{J_s}$, which is injected into the ferromagnet Py with the appropriate spin polarization required for antidamping torque. θ is the angle made by the direction of the in-plane applied field $\mathbf{H_0}$ relative to the x axis. (c) Four-magnon scattering mediated by thermally excited magnons $\omega_{\mathrm{th},i}$ and $\omega_{\mathrm{th},f}$ in equilibrium with thermal reservoir. $\omega_i + \omega_{\mathrm{th},i} = \omega_f + \omega_{\mathrm{th},f}$. (d) Four-magnon scattering by intermode interactions. $d\omega$ is the frequency shift within the mode caused by dipole or exchange interactions between ω_i and ω_j.

respect to the x axis of the microstrip line, we tune the eigenmodes of the spin waves defined by the spatial pattern of the internal field in Py, which is significantly modified by its dipolar, or demagnetizing, field.

Indeed, when the orientation of the applied field changes relative to the device edges, causing mode constriction, the spectral and spatial distributions of the resulting AO modes vary significantly. Figure 2(a) shows the angle θ dependence of the AO spectrum measured with bias current $I_{\mathrm{dc}} = 7$ mA at temperature $T = 77$ K in an applied field $H_0 = 570$ Oe. As θ increases, more excitation modes appear over a wider frequency range as a result of stronger mode constriction. We perform micromagnetic simulations using MUMAX3 [34](see Appendix B) to understand the complex spectra at various values of θ and to identify the relevant AO modes. Figure 2(b) shows the angle dependence of the AO spectra obtained from simulations conducted with the current-density distribution and Oersted field in Fig. 10. It describes the overall evolution of the experimental AO spectrum with increasing angle in Fig. 2(a) well, although more accurate spatial information reflecting the high-current-density nonlinearity and structural defects in the AO active region seems necessary to fully account for the details of the spectral shape. Figures

2(c)–2(g) show the spatial profiles of the spin-wave eigenmodes corresponding to the spectral peaks in Fig. 2(b) at various angles θ. We find that for $\theta \leq 65°$, the edge and bulk modes are combined, whereas for $\theta \geq 70°$, the edge and bulk modes are spatially separated due to the significant difference in the demagnetizing field between the edge and center regions. This separation also occurs spectrally [see Figs. 2(a) and 2(b)] and the largest AO peak appears in one of the bulk modes at frequencies higher than for the edge modes, which is in good agreement with previous AO results obtained on nanowires with $\theta = 85°$ [4].

The spectral and spatial mode profiles for AO in the active mode shown in Fig. 2 differ significantly from those of the linear spin-wave mode (see Fig. 6). This demonstrates that the dynamics of the AO mode are different from those of the linear spin-wave mode, arising from nonlinear effects such as complex bullet-mode dynamics involved with mode size reduction [1,3,35] or mode size oscillation [5,36]. In particular, this bullet-mode effect appears to be more pronounced in bulk modes 3a and 3b in Fig. 2(c) and bulk mode 3 in Fig. 2(d), away from the edge effect. The frequency jump as the signature of the bullet mode is also discussed in Appendix D.

In the evolution of the auto-oscillation modes with increasing bias current, we observe a transition in nonlinear damping due to mode-mode coupling. As can be seen in Fig. 3(a), obtained by measuring at $\theta = 65°$, as the current I_{dc}—and hence the antidamping torque—increases, the three main modes, C1, C2, and C3 [labeled in Fig. 3(e)], appear in the spectrum above each threshold current. We characterize these modes evolving at various values of I_{dc} with the resonance frequency f_0, the linewidth Δf, and the power P obtained from the Lorentzian fits, which are shown in Figs. 3(b)–3(d). Associated with the transition of nonlinear damping, we observe noticeable abrupt changes at the current $I_{\mathrm{MI}} = 7.1$ mA, such as the turnover from the linewidth narrowing to linewidth broadening (sign change of $\Delta f / I_{\mathrm{dc}}$) for all excitation modes [Fig. 3(c)] and power saturation in C1 mode [Fig. 3(d)]. This transition marks the onset of another relaxation process with additional damping. However, as I_{dc} increases in the high-current regime ($I_{\mathrm{dc}} > I_{\mathrm{MI}}$), we also observe (i) a monotonic red shift of the frequency for all three modes, reflecting a monotonic reduction in saturation magnetization due to magnon excitation [37] [Fig. 3(b)], (ii) a power increase in the C2 and C3 modes despite their linewidth broadening [Figs. 3(c) and 3(d)], and (iii) an increase in the total power [Fig. 3(d)]. All of these imply that the magnon population is growing faster than excited magnons can decay to other thermal reservoirs. Therefore, we conclude that nonlinear damping in the high-current regime occurs through magnon redistribution from low-frequency modes to high-frequency modes via nonlinear magnon-magnon scattering, as shown schematically in Figs. 1(c) or 1(d).
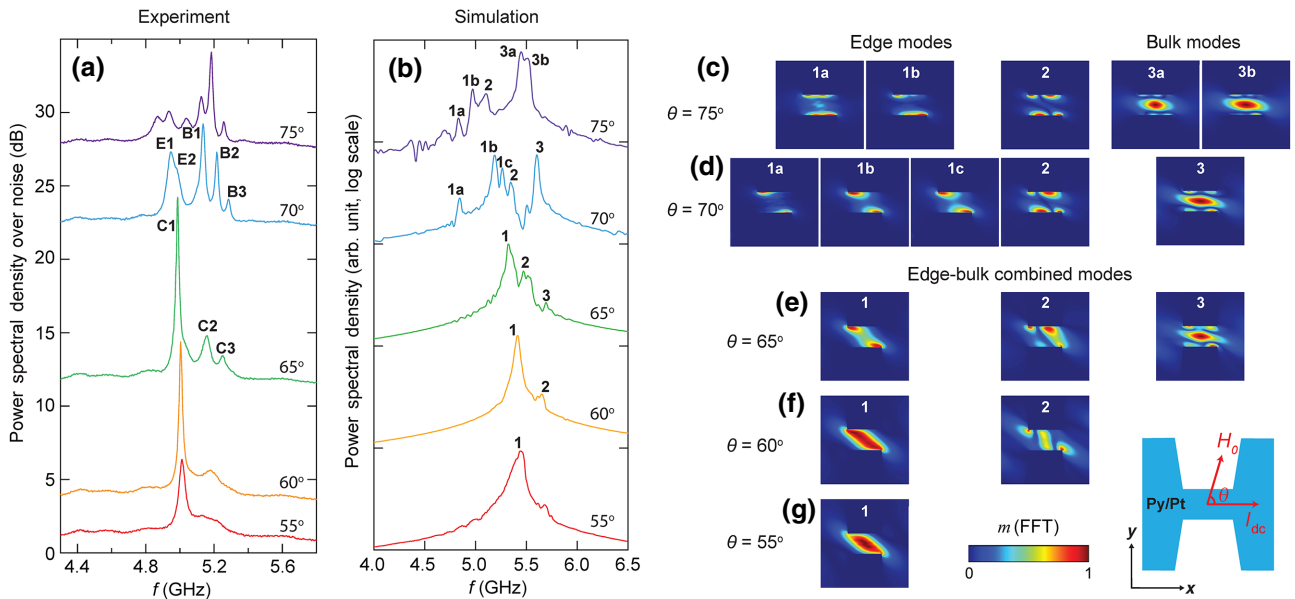
FIG. 2. (a) The angle dependence of the auto-oscillation spectrum, measured at $I_{dc} = 7$ mA, $T = 77$ K, and $H_0 = 570$ Oe. We vary the angle θ between $\mathbf{H_0}$ and I_{dc} in our experiments as shown in the diagram in the lower right corner of the figure. In the spectra for 65° and 70°, "C," "E," and "B" represent a combined edge-bulk mode, an edge mode, and a bulk mode, respectively. (b) Spectra for various values of θ obtained from micromagnetic simulations using MUMAX3, performed with the current-density distribution and Oersted field in Fig. 10. The corresponding I_{dc} are 7.92 mA for $\theta = 55°$, 7.26 mA for $\theta = 60°$, 6.92 mA for $\theta = 65°$, 6.52 mA for $\theta = 70°$, and 6.36 mA for $\theta = 75°$, about 0.2–0.3 mA larger than the respective threshold current at each value of θ. In (a) and (b), each spectrum is offset. (c)–(g) Spatial eigenmode profiles corresponding to the spectral peaks indicated by the numbers in (b) at various values of θ. The dynamic magnetization amplitude m is normalized on the color scale of each image. At $\theta = 70°$ and 75°, the spatial separation of the edge [(1) and (2)] modes and bulk (3) modes occurs as shown in (c) and (d), as well as their spectral separation as shown in (b).

There are other possible causes for the nonlinear damping transition at I_{MI}. The transition in the dependence of the power on the current shown in Fig. 3(d) may be described by the selective excitation and selective saturation of each mode. However, C2 and C3 in multimode excitation cannot be explained in this way, because their linewidth broadening, along with the power increase, at $I_{dc} \geq I_{MI}$ is not consistent with typical single-mode AO behavior, which exhibits linewidth narrowing with increasing I_{dc}, as C1 does for $I_{dc} < I_{MI}$. The power saturation of C1 may be caused by Joule heating or spin pumping. However, Joule heating cannot saturate the power of C1 without similarly affecting C2 and C3. Crucially, Joule heating can be observed in the spin-torque ferromagnetic resonance (ST FMR) by applying a high negative current ($I_{dc} < 0$) corresponding to positive damping, in which the spin-current-driven magnons are not generated. As the absolute value of $I_{dc} < 0$ increases, the decreasing resonance field can change to an increasing resonance field due to the decrease in saturation magnetization caused by Joule heating, similar to the previous Brillouin-light-scattering results [37]. However, this effect does not appear up to $I_{dc} = -8$ mA in our data (see Fig. 13), showing that Joule heating has a small effect. The intensity of spin pumping is proportional to the power of the AO mode [38]. As shown in Figs. 3(c) and 3(d), the linewidths of C1, C2,

and C3 with different powers start to increase together at I_{MI} with increasing I_{dc}, which cannot be explained by spin pumping. Therefore, we conclude that only mode-mode interaction can explain the coincidence of both the power transfer from C1 to the higher-frequency modes C2 and C3 and the turnover from linewidth broadening to linewidth narrowing of all three modes at I_{MI} for increasing I_{dc}, eventually leading to an almost even power distribution in the spectrum at 8 mA, as shown in Fig. 3(e).

In Fig. 4, we show the temperature dependence of the nonlinear damping of the AO system along with the threshold current I_{th} and transition current I_{MI}. Figure 4(a) shows the total power P_{total} summed for all excitation modes as a function of I_{dc} obtained at various temperatures for $\theta = 65°$. For each temperature, P_{total} has two current regimes, "A" for $I_{dc} < I_{MI}$, in which a single mode is dominant, and "B" for $I_{dc} \geq I_{MI}$, in which mode-mode interaction is active among multiple excitation modes, separated by the kink in P_{total} at which P in the lowest-frequency mode saturates. One of our findings is that the total power $P_{total,B}$ for all temperatures in regime B falls onto a single common curve [black line in Fig. 4(a)], whereas the total power $P_{total,A}$ in regime A is temperature dependent. This suggests that the mode-mode coupling occurs through a nonthermal process [Fig. 1(d)] originating from exchange or dipole interactions rather than thermally excited
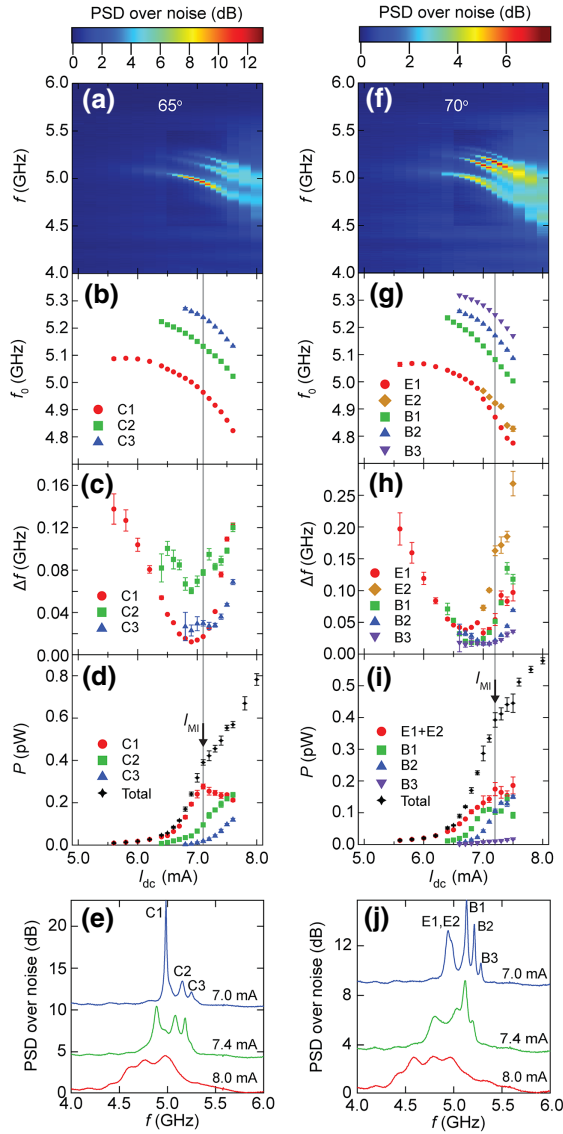
FIG. 3. (a) The evolution of the power spectral density (PSD) with increasing bias current I_{dc}, (b) the resonance frequency f_0 versus I_{dc}, (c) the linewidth Δf versus I_{dc}, and (d) the power P versus I_{dc} for the main modes C1, C2, and C3 for $\theta = 65°$. The ferromagnetic resonance (FMR) parameters in (b)–(d) are extracted by fitting the data in (a) to Lorentzian functions. (e) Representative spectra at high I_{dc} for $\theta = 65°$, showing the redistribution of power among modes at high I_{dc}. (f) The evolution of the PSD with increasing I_{dc}, (g) f_0 versus I_{dc}, (h) Δf versus I_{dc}, (i) P versus I_{dc} of the main edge (E1, E2) and bulk (B1, B2, B3) modes for $\theta = 70°$. The FMR parameters in (g)–(i) are extracted by fitting the data in (f) to Lorentzian functions. (j) Representative spectra at high I_{dc} for $\theta = 70°$, showing the redistribution of power among modes at high drive current. In (d) and (i), the black diamond markers are the total power P_{total} summed over all excited modes and I_{MI} represents the current at which the nonlinear damping transition occurs due to multimode interaction. At very high I_{dc}, the main modes shown here are not clearly identified due to the large linewidth broadening and the emergence of other excited modes, even though P_{total} can be obtained. Here, $H_0 = 570$ Oe and $T = 77$ K for all measurements.

magnon-mediated scattering [Fig. 1(c)]. The rapid growth of $P_{total,A}$ [colored lines in Fig. 4(a)] from each threshold current I_{th} is eventually limited by $P_{total,B}$ [black line in Fig. 4(a)] at each corresponding transition current I_{MI} for all temperatures. This indicates that the much faster relaxation process arising from the temperature-independent mode-mode interactions in regime B predominates over the temperature-dependent single-mode relaxation process occurring in regime A. Note that magnon thermalization through redistribution within the dynamic magnetic system is only possible if the relaxation via nonlinear magnon scattering arising from mode coupling is much faster than the relaxation to the external nonmagnetic systems in individual modes by intrinsic Gilbert damping or spin pumping.

In order to quantify the nonlinear damping of the AO system, we discuss the parameter Q, which represents the change in the positive nonlinear damping $\Gamma_+ \approx \Gamma_G (1 + Qp)$ with increasing AO power, where Γ_G is the Gilbert damping [39]. Q as well as I_{th} can be obtained from the relationship between the normalized AO power p and I_{dc} (see Appendix C). Figures 4(b) and 4(c) show the temperature dependence of the AO parameters in the regimes A and B discussed above: temperature-dependent Q_A, $I_{th,A}$, I_{MI}, and temperature-independent $Q_B, I_{th,B}$. The larger value of Q_B relative to Q_A observed in Fig. 4(b) indicates that the mode couplings in regime B cause additional nonlinear damping compared to regime A. In regime A, where the single mode C1 is dominant, Q_A depends on the temperature such that it is almost constant at $T \leq 125$ K but it increases for $T > 125$ K. This reflects the temperature dependence of the minimum linewidth and the maximum power of C1 in Figs. 4(g) and 4(h) and the existence of another temperature-independent relaxation mechanism below 125 K for an individual AO mode. Also, as T increases, both $I_{th,A}$ and I_{MI} decrease linearly, demonstrating that thermal fluctuation noise facilitates the generation and stabilization of the AO mode and of mode-mode coupling with the smaller I_{dc}, such as

$$I_{th}(T) = I_{th,0} + \kappa_{th}T, \qquad (1)$$

$$I_{MI}(T) = I_{MI,0} + \kappa_{MI}T, \qquad (2)$$

where $I_{th,0}$ and $I_{MI,0}$ are the intrinsic threshold and transition currents with the thermal fluctuation excitation effects removed and κ_{th} and κ_{MI} are coefficients with respect to temperature change. The temperature dependence of the intrinsic threshold, $I_{th,0}(T)$, can be obtained from a separately measured ST FMR, where $I_{th,0}$ is estimated to be almost constant in the temperature range of $5 - 300$ K (see Appendix E).

There are significant changes in the current evolution of the AO modes when θ changes from $65°$ to $70°$, as shown
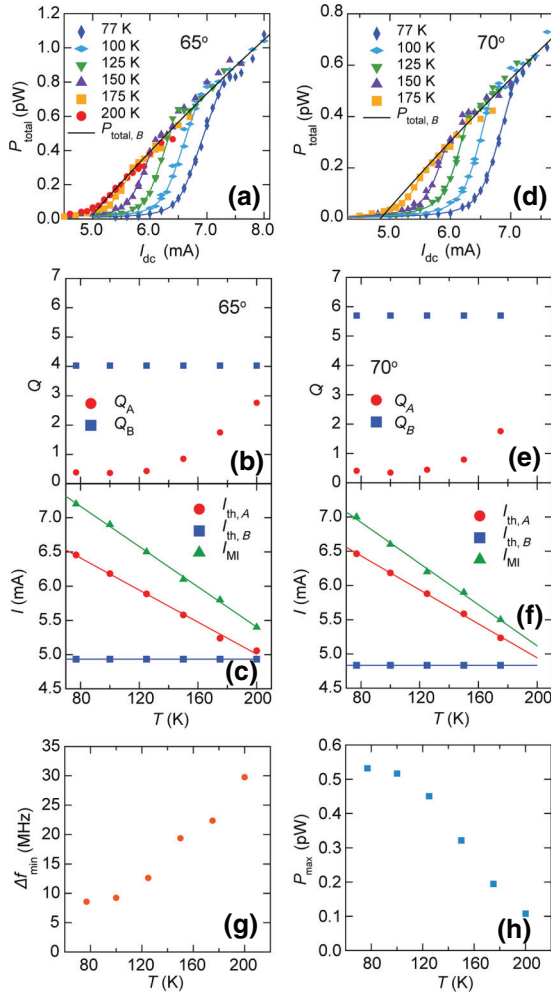
FIG. 4. (a) The total power P_{total} of the AO as a function of I_{dc} at various values of temperature T, (b) the nonlinear damping coefficient Q versus T, (c) the threshold current I_{th} versus T and the transition current I_{MI} versus T for $\theta = 65°$. The colored solid curves are the linear fits to Eq. (1) with $I_{\text{th},0} = 7.35$ mA and $\kappa_{\text{th}} = -0.0117$ mA/K and to Eq. (2) with $I_{\text{MI},0} = 8.34$ mA and $\kappa_{\text{MI}} = -0.0147$ mA/K for I_{th} and I_{MI}, respectively. Similarly, (d) the P_{total} of the AO as a function of I_{dc} at various values of T, (e) Q versus T, and (f) I_{th} versus T and I_{MI} versus T for $\theta = 70°$. The colored solid curves are the linear fits to Eq. (1) with $I_{\text{th},0} = 7.43$ mA and $\kappa_{\text{th}} = -0.0124$ mA/K and to Eq. (2) with $I_{\text{MI},0} = 8.12$ mA and $\kappa_{\text{MI}} = -0.015$ mA/K for I_{th} and I_{MI}, respectively. The colored solid curves in (a) and (d) are the P_{total} calculated using the theoretical equation [see Eq. (C4) in Appendix C] with Q_A and $I_{\text{th},A}$ in (b) and (c), and (e) and (f), respectively. The black curves in (a) and (d) are the P_{total} calculated using the theoretical equation [see Eq. (C5) in Appendix C] with the common values of Q_B and $I_{\text{th},B}$ in (b) and (c), and (e) and (f), respectively. Here, "A" represents the individual-mode-dominant regime ($I_{\text{dc}} < I_{\text{MI}}$) and "$B$" represents the mode-interaction-activation regime ($I_{\text{dc}} \geq I_{\text{MI}}$). The normalization factor $N_0 = 9.5$ pW and 8.7 pW, determined from fitting, for $\theta = 65°$ and $\theta = 70°$, respectively (see Appendix C) and $H_0 = 490$ Oe. The temperature dependence of (g) the minimum linewidth and (h) the maximum power of the C1 mode for $\theta = 65°$.

in Figs. 3(a) and 3(f). The edge-bulk combined modes (C1, C2, C3) at $\theta = 65°$ [see Figs. 2(e) and 3(a)–3(e)] are spectrally and spatially separated into edge (E1, E2) and bulk (B1, B2, B3) modes at $\theta = 70°$ [see Figs. 2(d) and 3(f)–3(j)]. As a result, for the AO modes existing at $\theta = 70°$ [see Figs. 3(g)–3(i)], the evolution of f_0, Δf, and P of the AO modes with increasing I_{dc} is more complex than for 65°: the E1 and E2 modes split at 7 mA and there can be various mode-mode couplings with different strengths of dipolar and exchange interactions depending on the spatial distance between the two interacting modes (e.g., edge-edge, edge-bulk, and bulk-bulk). This information can be valuable in developing strategies that employ spectral and spatial mode separation to reduce mode couplings and thus enhance the performance of auto-oscillators. We note that these mode couplings should be distinguishable from the nonlinear bullet-mode dynamics. The power sum of E1 and E2 monotonically increases up to $I_{\text{MI}} = 7.2$ mA until it saturates, creating a kink in P_{total} as shown in Fig. 3(i). The temperature dependence of the AO parameters for $\theta = 70°$ shown in Figs. 4(e) and 4(f) is generally similar to that for $\theta = 65°$, except for a further increased Q_B value, perhaps due to the increased number of intermode interaction routes allowed between a larger number of AO modes.

III. CONCLUSIONS

In conclusion, we observe the nonlinear damping transition of the auto-oscillation modes through the total power as a function of the drive current, which coincides with the onset of power distribution among multiple modes and linewidth broadening of all individual modes. We find the nonlinear damping due to mode-mode coupling to be independent of temperature, which suggests that the mode coupling occurs through intermode interactions such as dipole and exchange interactions rather than thermally excited magnon-mediated nonlinear scattering. This study of nonlinear damping due to mode couplings presents a promising pathway toward overcoming the current limitations of efficiently controlling mode interactions in spin Hall nano-oscillators to prevent mode crosstalk or intermode energy transfer and deepens the understanding of complex nonlinear spin dynamics in multimode spin-wave systems. As one solution, we can generate well-defined AO modes locally excited by the dipole field from a nano- or micron-scale permanent magnet [19], where the number of modes and their frequency distribution can be tuned by changing the local dipole field by moving a permanent magnet relative to the sample surface. Furthermore, the interaction between two spatially separated AOs can be controlled by adjusting the relative lateral distance in a scanned system [16–19].

APPENDIX A: ANGLE DEPENDENCE OF AUTO-OSCILLATION SPECTRUM OVER EXTENDED ANGLE RANGE

Figure 5 shows the dependence of the auto-oscillation spectrum on the angle, similar to Fig. 2(a) but over an extended angular range: $\theta = 50° - 85°$. At $\theta \leq 65°$, the lowest-frequency mode has the largest amplitude and it shifts slightly toward lower frequencies as θ increases. The mode starts to split and its amplitude decreases above $70°$ while the frequency shifts monotonically lower with increasing θ. On the other hand, the high-frequency modes hardly shift with increasing θ and at $\theta \geq 70°$, one of them has the largest amplitude among all excited AO modes in the spectrum instead of the lowest-frequency mode. Our micromagnetic simulations in Appendix B show that edge modes at low frequencies shift monotonically to lower frequencies, while bulk modes at high frequencies hardly shift; this characteristic behavior allows edge and bulk modes to be differentiated for $\theta \geq 70°$.

APPENDIX B: MICROMAGNETIC SIMULATIONS

We perform micromagnetic simulations using MUMAX3 [34] to understand the complex AO spectra and identify their relevant spatial mode profiles. In the simulations, the
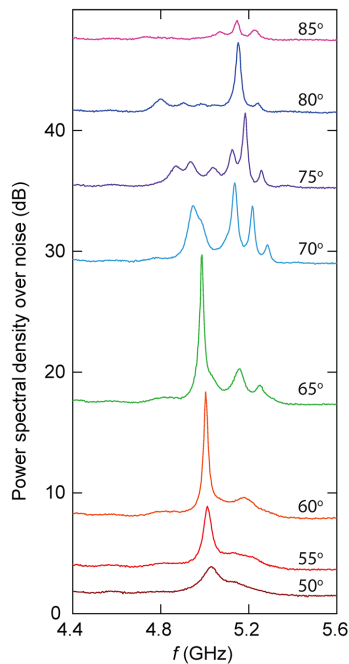

FIG. 5. The angle dependence of the auto-oscillation spectrum in Fig. 2(a) extended to a wide angle range. It is measured at $I_{dc} = 7$ mA, $T = 77$ K and $H_0 = 570$ Oe.

computational dimension 2.6 μm $\times$ 9 μm $\times$ 5 nm is subdivided into $5 \times 17.5 \times 5$ nm cells. As magnetic parameters, we use the gyromagnetic ratio of $\gamma/2\pi = 2.8$ MHz/G and the effective magnetization $4\pi M_{\mathrm{eff}} = 6502$ G obtained from the ST-FMR data (see Appendix D), measured at $I_{dc} = 0$ via the Kittel equation:

$$f_0 = \frac{\gamma}{2\pi} \left[H_0 \left(H_0 + 4\pi M_{\mathrm{eff}} \right) \right]^{1/2}. \tag{B1}$$

The standard values of the exchange stiffness $A_{\mathrm{ex}} = 1.3 \times 10^{-11}$ J/m and the Gilbert damping constant $\alpha = 0.01$ for permalloy are used.

1. Linear spin-wave eigenmode

First, we perform micromagnetic simulations in the linear regime of magnetodynamics with no bias current. Initially, the magnetic system is excited by a sinc rf field with an amplitude of 10 mT and a cutoff frequency of 40 GHz. Then, Gilbert damping is turned off by making $\alpha = 0$, allowing the magnetic dynamic system to proceed freely for 187 ns. We obtain the spectral and spatial profiles of the modes by performing Fourier transform with dynamic motion after 62 ns to avoid initial transients [9].

Figures 6(b)–6(f) show the spatial profile of the linear spin-wave eigenmodes corresponding to each spectral peak indicated by the number in Fig. 6(a) for each angle θ. The edge and bulk modes are combined for $\theta \leq 65°$, whereas the edge and bulk modes are spatially and spectrally separated for $\theta \geq 70°$ due to the significant difference in the demagnetizing field between the edge and center regions. Edge modes at low frequencies shift monotonically to lower frequencies and bulk modes at high frequencies shift little.

2. Self-oscillatory mode

The auto-oscillation mode of the system is obtained by solving the Landau-Lifshitz-Gilbert equation with an antidamping spin torque applied to the active region of the AO device. In the simulations, we try two different current-density distributions shown in Figs. 7 and 10, both considered for a 1-mA bias current.

As an initial state in the simulation, the magnetic system is allowed to relax to a state close to the ground state. The antidamping torque proportional to the current density in Figs. 7 and 10 scaled by the current value is activated at 0 ns. If this antidamping torque is smaller than the Gilbert damping, the magnetization oscillations decay, whereas if the antidamping torque is larger than the Gilbert damping, the magnetization oscillations grow until their amplitude saturates. We define a threshold current as that at which antidamping is balanced with Gilbert damping, where the magnetization oscillates with a constant amplitude over time. The scale factor for the current in the simulations
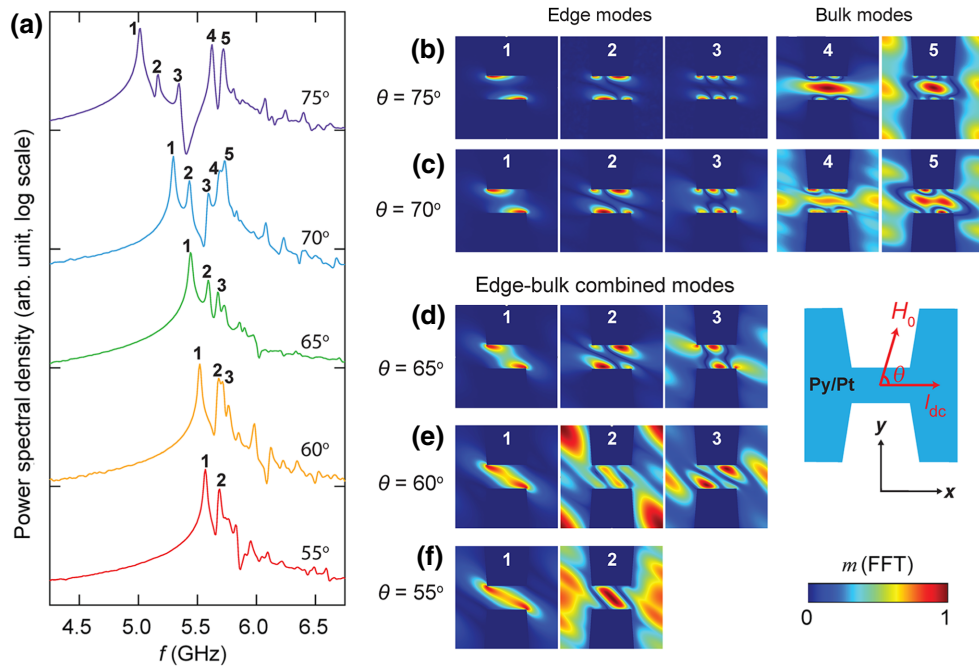
FIG. 6.   (a) Spectra for various values of θ obtained from the micromagnetic simulation using MUMAX3 with zero bias current, which reflect the linear spin-wave eigenmodes determined by the applied field $\mathbf{H_0}$ and the constricted sample geometry. This is in contrast to the case of nonlinear self-oscillatory modes with relatively larger amplitudes driven by the applied antidamping spin torque. In (a), each spectrum is vertically offset. (b)–(f) Spatial eigenmode profiles corresponding to the spectral peaks indicated by the numbers in (a) at various values of θ. The dynamic magnetization amplitude m is normalized on the color scale of each image. At $\theta = 70°$ and $75°$, the spatial separation of edge modes [(1)–(3)] and bulk modes [(4) and (5)] occurs, as shown in (b) and (c), as well as their spectral separation, as shown in (a).

is chosen so that the threshold currents in the simulations are as close as possible to the threshold currents in the actual experimental data. The spectral and spatial profiles of the excitation modes are obtained by performing Fourier transform of the time dependence of the magnetization dynamics.

a. Micromagnetic simulation using current-density distribution calculated in COMSOL

Figure 7 shows the current-density distribution of the AO system for a 1-mA current calculated using COMSOL [40] and the Oersted field produced by it. These determine the antidamping torque in the micromagnetic simulations and the corresponding results are shown in Figs. 8 and 9. Figures 8(a) and 8(b) show the evolution of the power spectral density (PSD) with increasing bias current I_{dc} for $\theta = 65°$ and $\theta = 70°$, respectively, and their representative line cuts are shown in Figs. 8(c) and 8(d), respectively. These simulation data show the key features of the experimental data in Fig. 3, such as monotonic red shift of the resonant frequency, mode-amplitude growth, and mode-amplitude saturation with increasing I_{dc}. In the simulation, the strong mode broadening starts at a relatively lower I_{dc} compared to the experimental data, so Fig. 8 shows

the simulation result applicable only to the low-current region of the experimental data in Fig. 3. This indicates that the nonlinear magnonic effect occurring at high currents, which can cause stronger self-excitation of the AO mode with high coherence, seems to be lacking in the simulations. Since thermal effects play no role in the simulations, the mode broadening seen at high I_{dc} arises purely from dipole or exchange spin-spin interactions of dynamic magnetization occurring at relatively large cone angles. This directly demonstrates the nonlinear damping due to mode couplings that occurs via dipole or exchange interactions, supporting the main conclusion of the paper.

Figure 9(a) shows the spectrum for various values of θ and Figs. 9(b)–9(f) show the spatial eigenmode profiles corresponding to the spectral peaks indicated by the numbers in Fig. 9(a). Most of the AO modes excited by the antidamping torque are edge modes that only shift to lower frequencies with increasing θ, while the barely shifted bulk modes shown in the linear spin-wave modes in Fig. 6 are mostly suppressed. Compared with the spatial mode profiles of the linear spin-wave modes in Fig. 6, the edge modes in this simulation seem to be selectively excited and evolved from the linear spin-wave modes by the inhomogeneous current-density distribution.
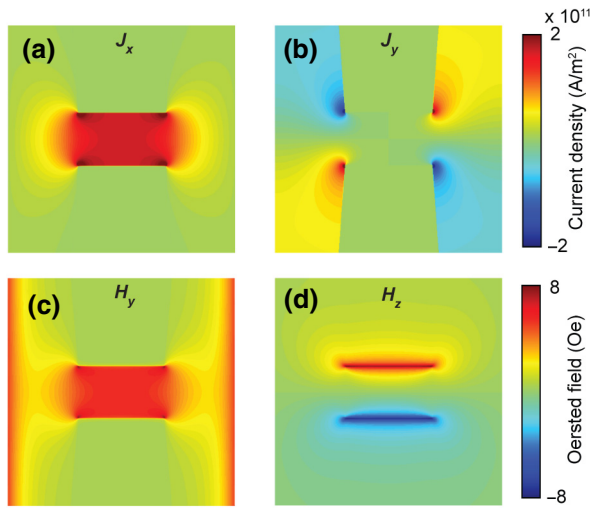
FIG. 7.   The COMSOL [40] calculation of the current densities in the AO structure for a 1-mA current: (a) the x component of the current-density distribution J_x, (b) the y component of the current-density distribution J_y, (c) the y component of the Oersted field H_y, and (d) the z component of the Oersted field H_z. $J_z = 0$ and $H_x = 0$. The antidamping spin torque in the micromagnetic simulations is calculated based on these maps: the corresponding results are shown in Figs. 8 and 9.

b. Micromagnetic simulation using current-density distribution of 2D Gaussian model

In order to test the effect of the inhomogeneous current-density distribution on the excitation of the AO modes in the simulation, we try a micromagnetic simulation using the different current-density distribution in Fig. 10(a), where the current density J_x has a 2D Gaussian distribution with a maximum at the center and a broader distribution as a function of the position in the device compared to Fig. 7(a) and $J_y = J_z = 0$. Indeed, the spectral shapes in this simulation are considerably different as shown in Fig. 2(b) and Figs. 11(c) and 11(d). In contrast to Fig. 9, bulk modes excited around the central region are unsuppressed for $\theta = 70°$ and $75°$ and can have larger mode amplitudes than edge modes, as shown in Fig. 2. These bulk modes exhibit improved agreement with experimentally observed AO modes; in particular, a small frequency shift with increasing θ, as shown in Figs. 2(a) and 5. Also, the overall spectral shapes associated with the number of excited AO modes, their relative frequencies and amplitudes, and their frequency-shift behavior for varying θ in Fig. 2(b) better match the experimental data in Fig. 2(a) compared to the other AO simulations in Figs. 6(a) and 9(a). Therefore, we conclude that the actual current-density distribution is closer to the 2D Gaussian function in Fig. 10 than that calculated using COMSOL in Fig. 7. We note that unidentified structural defects around the edges of the AO active region of the sample can significantly alter the
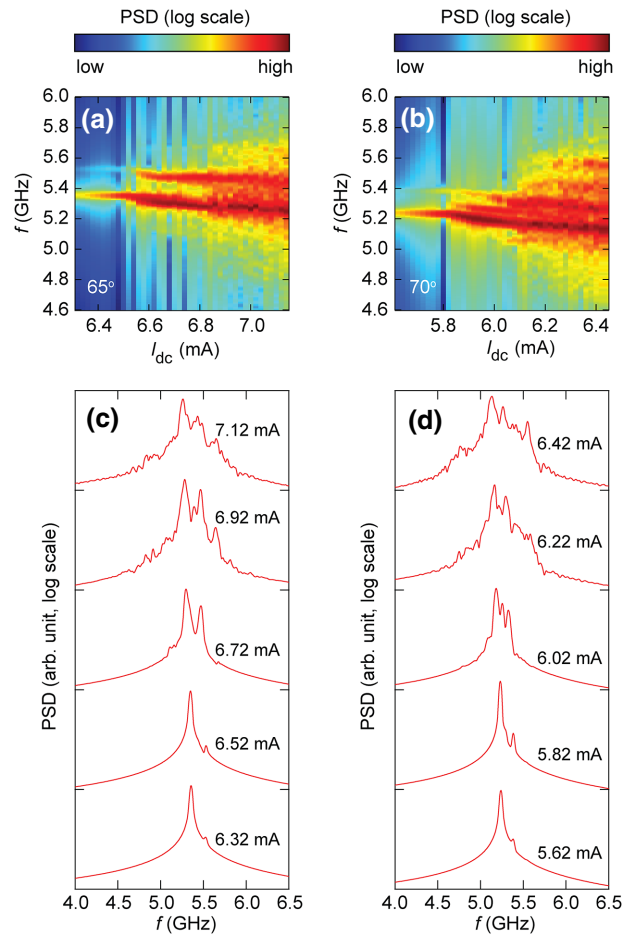

FIG. 8.   The evolution of the PSD with increasing bias current I_{dc} for (a) $\theta = 65°$ and (b) $\theta = 70°$, obtained from micromagnetic simulations performed with the current-density distribution and Oersted field in Fig. 7. (c) Representative spectrum line cuts in (a) for various values of I_{dc} at $\theta = 65°$. (d) Representative spectral line cuts in (b) for various values of I_{dc} at $\theta = 70°$.

spectral shapes, especially for $\theta = 70°$ and $75°$, where the mode-constriction effect is stronger.

This conclusion is further supported by the evolution of the PSD with increasing bias current I_{dc} for $\theta = 65°$ and $70°$, shown in Figs. 11(a) and 11(b), respectively. In Figs. 11(a) and 11(c) for $\theta = 65°$, the edge mode at the lowest frequency has the largest amplitude at any I_{dc}, whereas in Figs. 11(b) and 11(d) for $\theta = 70°$, the bulk mode at approximately 5.6 GHz grows with increasing I_{dc} and eventually has a larger amplitude than any edge modes located at the lower frequencies at high I_{dc}, which agrees well with our experimental data in Fig. 3.

APPENDIX C: QUANTIFYING NONLINEAR DAMPING WITH THE COEFFICIENT Q

The nonlinear single-mode auto-oscillator can be described with a universal oscillator model, another form
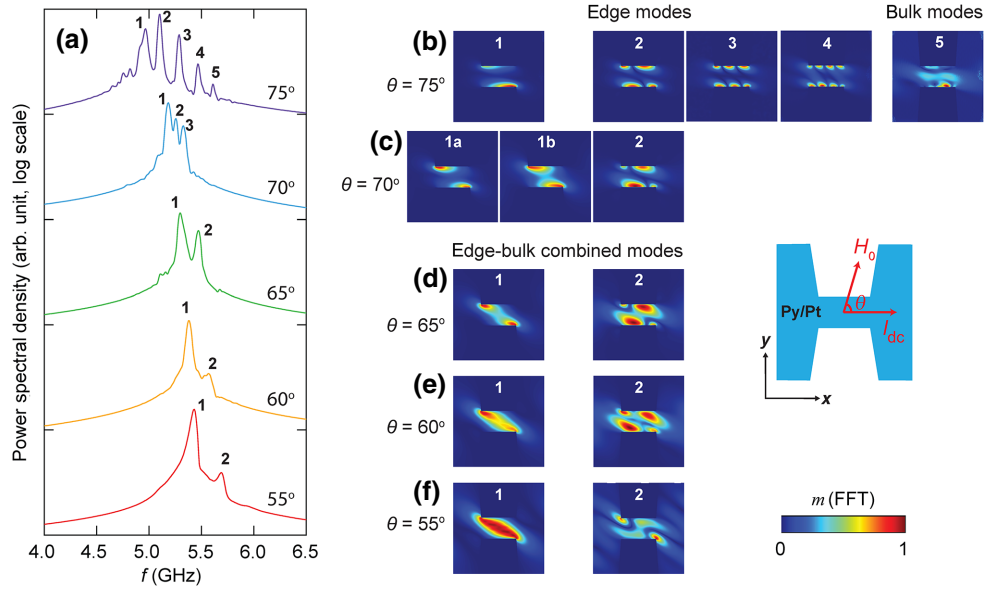
FIG. 9. (a) Spectra for various values of θ obtained from micromagnetic simulations using MUMAX3, performed with the current-density distribution and Oersted field in Fig. 7. The corresponding I_{dc} are 8.28 mA for $\theta = 55°$, 7.42 mA for $\theta = 60°$, 6.72 mA for $\theta = 65°$, 6.02 mA for $\theta = 70°$, and 5.58 mA for $\theta = 75°$, 0.2 mA larger than the respective threshold current at each value of θ. Each spectrum is vertically offset for clarity. (b)–(f) Spatial eigenmode profiles corresponding to the spectral peaks indicated by numbers in (a) at various values of θ. The dynamic magnetization amplitude m is normalized on the color scale of each image. At $\theta = 70°$ and 75°, the spatial separation of edge [(1)–(4)] and bulk (5) modes occurs, as shown in (b) and (c), as well as their spectral separation, as shown in (a). Compared to the linear spin-wave modes in Fig. 6, the bulk modes are mostly suppressed in this simulation.

of the Landau-Lifshitz equation, derived by Slavin and Tiberkevich [39]:

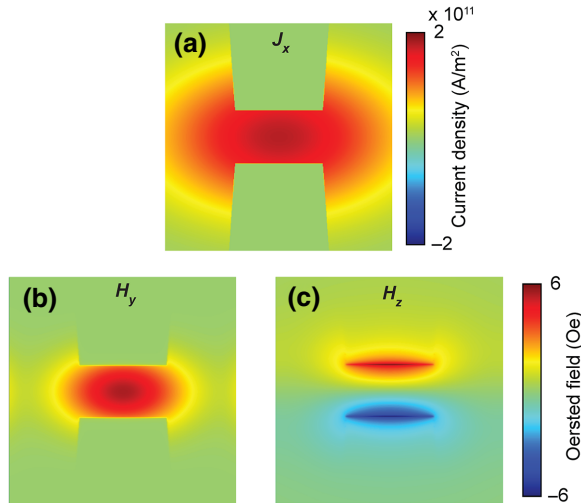$$\frac{dc}{dt} + i\omega(p)c + \Gamma_+(p)c - \Gamma_-(p)c = f_n(t), \qquad (C1)$$

FIG. 10. (a) The x component of the current-density distribution J_x, (b) the y component of the Oersted field H_y, and (c) the z component of the Oersted field H_z in the AO system for the 1-mA current used to apply antidamping spin torque in the micromagnetic simulations. $J_y = J_z = 0$ and $H_x = 0$. The corresponding results are shown in Figs. 2 and 8.

where c is the complex dimensionless dynamic magnetization amplitude, p $(= |c|^2)$ is the oscillation power, $\omega(p)$ is the power-dependent nonlinear frequency,

$$\Gamma_+(p) \approx \Gamma_G(1 + Qp), \qquad (C2)$$

$$\Gamma_-(p) \approx \sigma I(1 - p), \qquad (C3)$$

are the positive and negative damping constant, respectively, $f_n(t)$ is the thermal fluctuation noise, Γ_G $(= \alpha\omega)$ is the Gilbert damping, Q is the nonlinear damping coefficient, σ is the spin-current efficiency, and I is the drive current. On the left-hand side of Eq. (C1), the second term describes precession, the third term describes damping, and the fourth term describes antidamping. Note that $\omega(p)$, $\Gamma_+(p)$, and $\Gamma_-(p)$ are auto-oscillation power p dependent.

In order to describe the nonlinear damping of the multimode AO system in a simple and quantitative way, we calculate Q from the relationship with $P_{\text{total}} = N_0 p$, where for $I_{dc} < I_{MI}$,

$$p = \frac{Q\eta}{Q + \eta}\left[1 + \frac{\exp(-(\zeta + Q)/Q^2\eta)}{E_\beta((\zeta + Q)/Q^2\eta)}\right] + \frac{\zeta - 1}{\zeta + Q}, \quad (C4)$$

and for $I_{dc} \geq I_{MI}$,
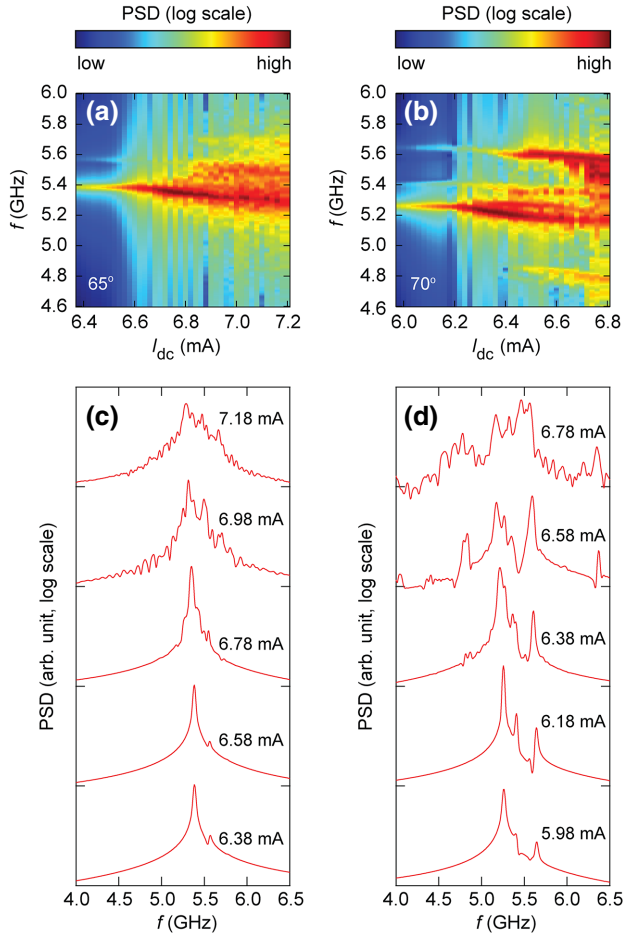
$$p = \frac{\zeta - 1}{\zeta + Q}. \qquad (C5)$$

FIG. 11.   The evolution of the PSD with increasing bias current I_{dc} for (a) $\theta = 65°$ and (b) $\theta = 70°$, obtained from micromagnetic simulations performed with the current-density distribution and Oersted field in Fig. 10. (c) Representative spectrum line cuts in (a) for various values of I_{dc} at $\theta = 65°$. (d) Representative spectrum line cuts in (b) for various values of I_{dc} at $\theta = 70°$.

In these expressions, N_0 is the power-conversion factor for the normalized p, $\zeta = I/I_{th}$, I_{th} is the threshold current, η is the effective noise power, $E_\beta(x) = \int_1^\infty e^{-xt}/t^\beta dt$, and $\beta = -(1 + Q)\zeta/Q^2\eta$ [39]. Note that the Slavin-Tiberkevich model was originally intended to describe single-mode auto-oscillators, so Q in the multimode excitation regime of $I_{dc} \geq I_{MI}$ is an "effective" nonlinear damping parameter of the entire AO system. We also obtain η in Eq. (C4) along with other AO parameters presented in Fig. 4 by fitting but Fig. 12 does not show a clear temperature dependence on η.

APPENDIX D: SPIN-TORQUE FERROMAGNETIC RESONANCE

Figure 13(a) shows a typical ST-FMR spectrum measured at various direct currents I_{dc} ranging from -8 mA to
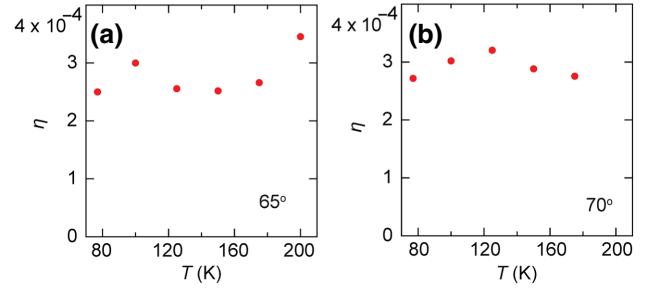

FIG. 12.   The noise level η versus the temperature T for (a) $\theta = 65°$ and (b) $\theta = 70°$, obtained from the fitting curves of the solid colored lines in Figs. 4(a) and 4(d).

8 mA. As the absolute value of $I_{dc} < 0$ increases, the ST-FMR peak broadens due to the enhanced damping, while as $I_{dc} > 0$ increases, the mode becomes narrower due to antidamping and eventually splits into a couple of modes. In order to see the overall shift of the ST-FMR peak, we normalize the signal V_{mix} to the maximum at each I_{dc}, which is shown in Fig. 13(b). With increasing $I_{dc} > 0$, the ST-FMR peak shifts to the higher field, because as the amplitudes of the self-localized AO modes grow, the static magnetization decreases. On the other hand, as the absolute value of $I_{dc} < 0$ increases up to -8 mA, the ST-FMR peak shifts monotonically to the lower field and does not show a shift to the higher field that might occur due to the decrease in saturation magnetization by Joule heating. This means that even at $I_{dc} = 8$ mA, regardless of its sign, the magnetic system of our device does not reach the current
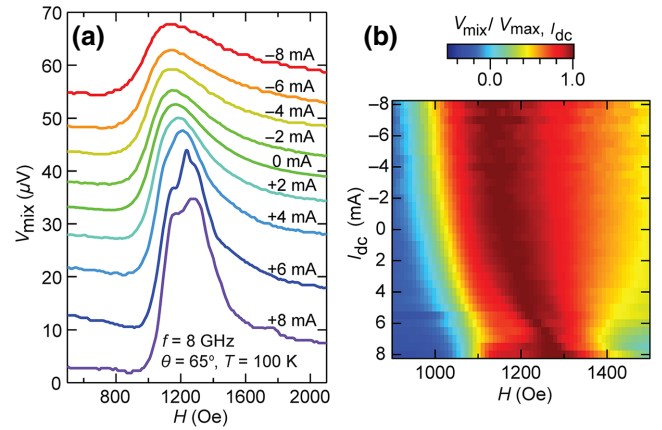

FIG. 13.   (a) The ST-FMR spectrum at various values of I_{dc} ranging from -8 mA to 8 mA. (b) The direct-current evolution of ST FMR, where the signal V_{mix} is normalized to the maximum at each I_{dc} to see the shift of the ST-FMR peak. Obviously, the monotonic ST-FMR peak shift to the lower field with no change in the shift to the higher field for the intensity of $I_{dc} < 0$ increasing up to -8 mA indicates no reduction in saturation magnetization that can be caused by Joule heating at a large intensity of I_{dc}.
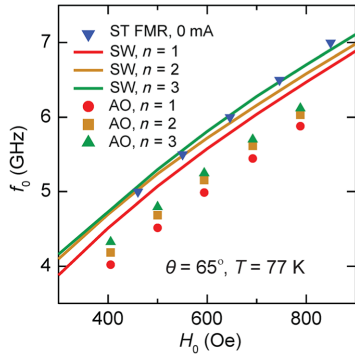
FIG. 14. The magnetic field dependence of the resonance frequency obtained in (i) the main mode of ST FMR measured at $I_{dc} = 0$ mA (blue inverted triangle), (ii) the auto-oscillation (AO) modes of $n = 1$ (red circle), $n = 2$ (square orange), and $n = 3$ (green triangle) measured at $I_{dc} = -7$ mA, and (iii) the linear spin-wave (SW) eigenmodes (red, orange, and green solid lines for $n = 1, 2, 3$ respectively), obtained in the micromagnetic simulations using MUMAX3 with $I_{dc} = 0$ mA and $4\pi M_s = 6.5$ kG. The frequency discrepancy of approximately 0.5 GHz between the linear spin-wave modes and the AO mode can be explained by the static magnetization reduction and the frequency jump near the onset I_{th} that has been observed in the literature as a feature of self-localization in the nonlinear "bullet" modes.

regime where the saturation magnetization decreases by Joule heating [37]. This provides crucial evidence that the contribution of Joule heating to the nonlinear damping of the AO system described in the main text is not significant at high I_{dc} up to 8 mA.

Figure 14 shows the resonance frequency f_0 of the auto-oscillation as a function of the applied magnetic field H_0 compared to the linear spin-wave eigenmode frequency and the resonance frequency of ST FMR at $I_{dc} = 0$ mA. The AO mode appears below the corresponding linear spin-wave mode with a discrepancy of approximately 0.5 GHz due to two contributions: one, by approximately 0.2 GHz, is the reduction of static magnetization due to the increased cone angle shown in Figs. 3(b) and 3(g); and the other, by approximately 0.3 GHz, is the frequency jump of the AO mode from the linear spin-wave mode frequency occurring near the onset I_{th}. The latter has been observed as the signature of the bullet mode in self-localization [1,3,35].

APPENDIX E: TEMPERATURE DEPENDENCE OF THE INTRINSIC THRESHOLD CURRENT

The threshold current I_{th} that we obtain from measurement of the AO power has two contributions as expressed in Eq. (1): (i) that due to thermal fluctuation, $\kappa_{th}T$, and (ii) an intrinsic threshold current $I_{th,0}$ arising from the antidamping torque due to the applied spin current. Here, we estimate the temperature dependence of the intrinsic threshold current $I_{th,0}(T)$ from the ST-FMR data.
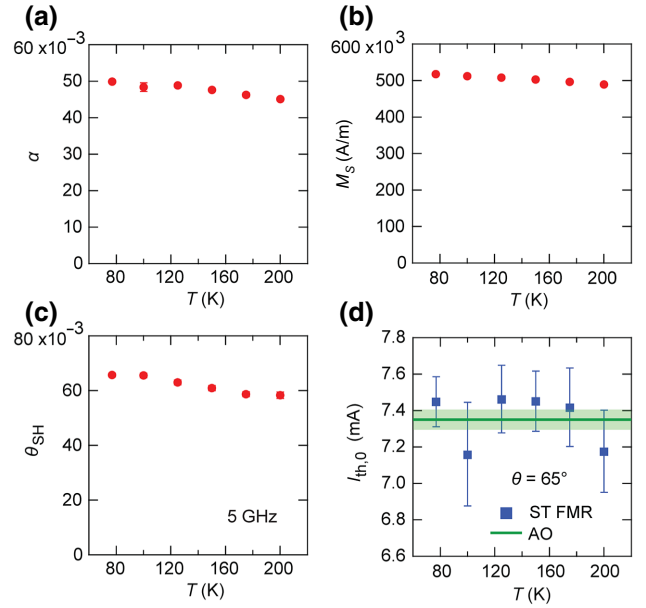

FIG. 15. The temperature dependence of (a) the Gilbert damping constant α, (b) the saturation magnetization M_S ($\simeq M_{eff}$), and (c) the spin Hall angle θ_{SH}, obtained from ST FMR. (d) The temperature dependence of the intrinsic threshold current $I_{th,0}$ induced by the spin Hall effect estimated by Eq. (E3), with parameters obtained from the ST FMR in (a)–(c), in comparison with that estimated from the AO data in Fig. 4(c).

According to the Slavin-Tiberkevich theory described in Appendix C, the intrinsic $I_{th,0}$ arising from the spin Hall effect is given by

$$I_{th,0} = \frac{\alpha\omega}{\sigma}. \tag{E1}$$

The spin-current efficiency σ is proportional to the temperature-dependent θ_{SH}/M_S in our AO system [41]:

$$\sigma(T) \propto \frac{\theta_{SH}(T)}{M_S(T)}. \tag{E2}$$

From Eqs. (E1) and (E2), the intrinsic threshold is given as

$$I_{th,0}(T) = C\frac{\alpha(T)M_S(T)}{\theta_{SH}(T)}, \tag{E3}$$

where C is a temperature-independent constant. θ_{SH} has been found to be temperature independent with a value of 0.068 for 13–300 K [42], and α for Py film with same thickness of 5 nm is also almost constant in the temperature range of 5–300 K, regardless of the capping materials, even though there is a slight temperature dependence of the surface damping around 50 K [43]. Also, M_S can be considered to be almost constant at $T \ll T_C$. Therefore, $I_{th,0}$ can be taken to be almost constant for varying temperature. Based on this, we express $I_{th}(T)$ determined from our

AO power in Fig. 4 as a simple sum of the temperature-independent $I_{th,0}$ and an additional thermal-fluctuation contribution that decreases linearly with temperature as in Eq. (1). We also measure almost constant α, M_S, and θ_{SH} from ST FMR in the temperature range of 77–200 K, as shown in Figs. 15(a)–15(c), and Fig. 15(d) shows our estimated temperature dependence of the intrinsic threshold $I_{th,0}(T)$, which is almost constant over the temperature within our estimation uncertainty.

---

[1] V. E. Demidov, S. Urazhdin, H. Ulrichs, V. Tiberkevich, A. Slavin, D. Baither, G. Schmitz, and S. O. Demokritov, Magnetic nano-oscillator driven by pure spin current, Nat. Mater. **11**, 1028 (2012).

[2] R. H. Liu, W. L. Lim, and S. Urazhdin, Spectral Characteristics of the Microwave Emission by the Spin Hall Nano-Oscillator, Phys. Rev. Lett. **110**, 147601 (2013).

[3] V. E. Demidov, S. Urazhdin, A. Zholud, A. V. Sadovnikov, and S. O. Demokritov, Nanoconstriction-based spin-Hall nano-oscillator, Appl. Phys. Lett. **105**, 172410 (2014).

[4] Z. Duan, A. Smith, L. Yang, B. Youngblood, J. Lindner, V. E. Demidov, S. O. Demokritov, and I. N. Krivorotov, Nanowire spin torque oscillator driven by spin orbit torques, Nat. Commun. **5**, 5616 (2014).

[5] L. Yang, R. Verba, V. Tiberkevich, T. Schneider, A. Smith, Z. Duan, B. Youngblood, K. Lenz, J. Lindner, A. N. Slavin, and I. N. Krivorotov, Reduction of phase noise in nanowire spin orbit torque oscillators, Sci. Rep. **5**, 16942 (2015).

[6] M. Collet, X. de Milly, O. d'Allivy Kelly, V. V. Naletov, R. Bernard, P. Bortolotti, J. Ben Youssef, V. E. Demidov, S. O. Demokritov, J. L. Prieto, M. Munoz, V. Cros, A. Anane, G. de Loubens, and O. Klein, Generation of coherent spin-wave modes in yttrium iron garnet microdiscs by spin-orbit torque, Nat. Commun. **7**, 10377 (2016).

[7] H. Mazraati, S. Chung, A. Houshang, M. Dvornik, L. Piazza, F. Qejvanaj, S. Jiang, T. Q. Le, J. Weissenrieder, and J. Åkerman, Low operational current spin Hall nano-oscillators based on NiFe/W bilayers, Appl. Phys. Lett. **109**, 242402 (2016).

[8] A. A. Awad, P. Durrenfeld, A. Houshang, M. Dvornik, E. Iacocca, R. K. Dumas, and J. Åkerman, Long-range mutual synchronization of spin Hall nano-oscillators, Nat. Phys. **13**, 292 (2017).

[9] M. Dvornik, A. A. Awad, and J. Åkerman, Origin of Magnetization Auto-Oscillations in Constriction-Based Spin Hall Nano-Oscillators, Phys. Rev. Appl. **9**, 014017 (2018).

[10] H. Mazraati, S. R. Etesami, S. A. H. Banuazizi, S. Chung, A. Houshang, A. A. Awad, M. Dvornik, and J. Åkerman, Auto-Oscillating Spin-Wave Modes of Constriction-Based Spin Hall Nano-Oscillators in Weak In-Plane Fields, Phys. Rev. Appl. **10**, 054017 (2018).

[11] H. Fulara, M. Zahedinejad, R. Khymyn, A. A. Awad, S. Muralidhar, M. Dvornik, and J. Åkerman, Spin-orbit torque–driven propagating spin waves, Sci. Adv. **5**, eaax8467 (2019).

[12] M. Haidar, A. A. Awad, M. Dvornik, R. Khymyn, A. Houshang, and J. Åkerman, A single layer spin-orbit torque nano-oscillator, Nat. Commun. **10**, 2362 (2019).

[13] C. Safranski, E. A. Montoya, and I. N. Krivorotov, Spin-orbit torque driven by a planar Hall current, Nat. Nanotechnol. **14**, 27 (2019).

[14] M. Zahedinejad, A. A. Awad, S. Muralidhar, R. Khymyn, H. Fulara, H. Mazraati, M. Dvornik, and J. Åkerman, Two-dimensional mutually synchronized spin Hall nano-oscillator arrays for neuromorphic computing, Nat. Nanotechnol. **15**, 47 (2020).

[15] R. V. Verba, V. S. Tiberkevich, and A. N. Slavin, Dipole-dominated dissipative magnetic solitons in quasi-one-dimensional spin-torque oscillators, Low Temp. Phys. **46**, 773 (2020).

[16] I. Lee, Y. Obukhov, G. Xiang, A. Hauser, F. Yang, P. Banerjee, D. V. Pelekhov, and P. C. Hammel, Nanoscale scanning probe ferromagnetic resonance imaging using localized modes, Nature **466**, 845 (2010).

[17] I. Lee, Y. Obukhov, A. J. Hauser, F. Y. Yang, D. V. Pelekhov, and P. C. Hammel, Nanoscale confined mode ferromagnetic resonance imaging of an individual $Ni_{81}Fe_{19}$ disk using magnetic resonance force microscopy (invited), J. Appl. Phys. **109**, 07D313 (2011).

[18] C. Zhang, Y. Pu, S. A. Manuilov, S. P. White, M. R. Page, E. C. Blomberg, D. V. Pelekhov, and P. C. Hammel, Engineering the Spectrum of Dipole Field-Localized Spin-Wave Modes to Enable Spin-Torque Antidamping, Phys. Rev. Appl. **7**, 054019 (2017).

[19] C. Zhang, I. Lee, Y. Pu, S. A. Manuilov, D. V. Pelekhov, and P. C. Hammel, Spin-orbit torque nano-oscillators by dipole-field-localized spin wave modes, Nano. Lett. **21**, 10208 (2021).

[20] S. Bonetti, V. Tiberkevich, G. Consolo, G. Finocchio, P. Muduli, F. Mancoff, A. Slavin, and J. Åkerman, Experimental Evidence of Self-Localized and Propagating Spin Wave Modes in Obliquely Magnetized Current-Driven Nanocontacts, Phys. Rev. Lett. **105**, 217204 (2010).

[21] P. K. Muduli, O. G. Heinonen, and J. Åkerman, Decoherence and Mode Hopping in a Magnetic Tunnel Junction Based Spin Torque Oscillator, Phys. Rev. Lett. **108**, 207203 (2012).

[22] P. K. Muduli, O. G. Heinonen, and J. Åkerman, Temperature dependence of linewidth in nanocontact based spin torque oscillators: Effect of multiple oscillatory modes, Phys. Rev. B **86**, 174408 (2012).

[23] S. Bonetti, V. Puliafito, G. Consolo, V. S. Tiberkevich, A. N. Slavin, and J. Åkerman, Power and linewidth of propagating and localized modes in nanocontact spin-torque oscillators, Phys. Rev. B **85**, 174427 (2012).

[24] O. G. Heinonen, P. K. Muduli, E. Iacocca, and J. Akerman, Decoherence, mode hopping, and mode coupling in spin torque oscillators, IEEE Trans. Magn. **49**, 4398 (2013).

[25] E. Iacocca, O. Heinonen, P. K. Muduli, and J. Åkerman, Generation linewidth of mode-hopping spin torque oscillators, Phys. Rev. B **89**, 054402 (2014).

[26] S. S.-L. Zhang, Y. Zhou, D. Li, and O. Heinonen, Mode coupling in spin torque oscillators, J. Magn. Magn. Mater. **414**, 227 (2016).

[27] J. C. Sankey, I. N. Krivorotov, S. I. Kiselev, P. M. Braganca, N. C. Emley, R. A. Buhrman, and D. C. Ralph, Mechanisms limiting the coherence time of spontaneous magnetic oscillations driven by dc spin-polarized currents, Phys. Rev. B **72**, 224427 (2005).

[28] R. K. Dumas, E. Iacocca, S. Bonetti, S. R. Sani, S. M. Mohseni, A. Eklund, J. Persson, O. Heinonen, and J. Åkerman, Spin-Wave-Mode Coexistence on the Nanoscale: A Consequence of the Oersted-Field-Induced Asymmetric Energy Landscape, Phys. Rev. Lett. **110**, 257202 (2013).

[29] E. Iacocca, P. Dürrenfeld, O. Heinonen, J. Åkerman, and R. K. Dumas, Mode-coupling mechanisms in nanocontact spin-torque oscillators, Phys. Rev. B **91**, 104405 (2015).

[30] I. Barsukov, H. K. Lee, A. A. Jara, Y.-J. Chen, A. M. Goncalves, C. Sha, J. A. Katine, R. E. Arias, B. A. Ivanov, and I. N. Krivorotov, Giant nonlinear damping in nanoscale ferromagnets, Sci. Adv. **5**, eaav6943 (2019).

[31] A. Etesamirad, R. Rodriguez, J. Bocanegra, R. Verba, J. Katine, I. N. Krivorotov, V. Tyberkevych, B. Ivanov, and I. Barsukov, Controlling magnon interaction by a nanoscale switch, ACS Appl. Mater. Interfaces **13**, 20288 (2021).

[32] F. M. de Aguiar, A. Azevedo, and S. M. Rezende, Theory of a two-mode spin torque nanooscillator, Phys. Rev. B **75**, 132404 (2007).

[33] S. S.-L. Zhang, E. Iacocca, and O. Heinonen, Tunable Mode Coupling in Nanocontact Spin-Torque Oscillators, Phys. Rev. Appl. **8**, 014034 (2017).

[34] A. Vansteenkiste, J. Leliaert, M. Dvornik, M. Helsen, F. Garcia-Sanchez, and B. Van Waeyenberge, The design and verification of MuMax3, AIP Adv. **4**, 107133 (2014).

[35] A. Slavinand and V. Tiberkevich, Spin Wave Mode Excited by Spin-Polarized Current in a Magnetic Nanocontact is a Standing Self-Localized Wave Bullet, Phys. Rev. Lett. **95**, 237201 (2005).

[36] K. Wagner, A. Smith, T. Hache, J.-R. Chen, L. Yang, E. Montoya, K. Schultheiss, J. Lindner, J. Fassbender, I. Krivorotov, and H. Schultheiss, Injection locking of multiple auto-oscillation modes in a tapered nanowire spin Hall oscillator, Sci. Rep. **8**, 16040 (2018).

[37] V. E. Demidov, S. Urazhdin, E. R. J. Edwards, M. D. Stiles, R. D. McMichael, and S. O. Demokritov, Control of Magnetic Fluctuations by Spin Current, Phys. Rev. Lett. **107**, 107204 (2011).

[38] M. B. Jungfleisch, A. V. Chumak, A. Kehlberger, V. Lauer, D. H. Kim, M. C. Onbasli, C. A. Ross, M. Kläui, and B. Hillebrands, Thickness and power dependence of the spin-pumping effect in $Y_3Fe_5O_{12}$/Pt heterostructures measured by the inverse spin Hall effect, Phys. Rev. B **91**, 134407 (2015).

[39] A. Slavinand and V. Tiberkevich, Nonlinear auto-oscillator theory of microwave generation by spin-polarized current, IEEE Trans. Magn. **45**, 1875 (2009).

[40] C. Inc., COMSOL (2019).

[41] L. Liu, T. Moriyama, D. C. Ralph, and R. A. Buhrman, Spin-Torque Ferromagnetic Resonance Induced by the Spin Hall Effect, Phys. Rev. Lett. **106**, 036601 (2011).

[42] Y. Wang, P. Deorani, X. Qiu, J. H. Kwon, and H. Yang, Determination of intrinsic spin Hall angle in Pt, Appl. Phys. Lett. **105**, 152412 (2014).

[43] Y. Zhao, Q. Song, S.-H. Yang, T. Su, W. Yuan, S. S. P. Parkin, J. Shi, and W. Han, Experimental investigation of temperature-dependent Gilbert damping in permalloy thin films, Sci. Rep. **6**, 22890 (2016).